A High-Order-Harmonic Compound-Rotor Based Brushless Doubly-Fed Machine for Variable Speed Constant Frequency Wind Power Generation

Mingyuan Jiang, Shuangxia Niu, *Senior Member, IEEE*, and C.C. Chan, *Life Fellow, IEEE*

***Abstract*—This paper addresses the issue of relatively inferior torque performance in brushless doubly fed machines (BLDFMs) used for variable speed constant frequency (VSCF) operation in wind power generation systems. To mitigate this limitation, a novel brushless dual-electrical-port dual-mechanical-port DFM (BLDD-DFM) structure is proposed, which employs high-order harmonic modulation to reduce energy consumption in the control winding during VSCF applications. The compound outer rotor is designed specifically to enhance the third-harmonic component within the inner airgap's magnetomotive force. By implementing high-order harmonic modulation, the slip ratio is reduced, resulting in over a 3-fold decrease in energy consumption compared to conventional designs. Additionally, under rated conditions, the proposed design exhibits maximum torque improvements of 23.03% for the outer rotor torque and 144.08% for the inner rotor torque compared to the conventional design. Finite element analysis and comparative studies with existing counterparts validate the effectiveness of the proposed machine. Furthermore, a prototype is presented to demonstrate the feasibility and advantages of the proposed design.**

***Index Terms*—Brushless doubly fed machines, High-order-harmonic modulation, Variable speed constant frequency, Wind power generation**

I. Introduction

With escalating environmental concerns and the prevailing energy crisis, there has been a notable shift towards substituting power generation systems reliant on fossil fuels with renewable energy sources [1, 2]. Within this context, wind power generation systems have garnered significant attention within the industrial sector, experiencing rapid advancements over the past few decades due to their cost-effectiveness and sustainable nature.

Given the inherent variability of wind speeds due to natural factors, maintaining a consistent frequency in the electrical output port call for the development of specific technologies. These technologies, referred as variable speed constant frequency (VSCF) operation, enable wind power generation systems to sustain a constant industrial frequency in the output electrical port, regardless of fluctuations in the input speed of the mechanical port [3].

Doubly fed machine (DFM) is a commonly employed method in industrial applications to achieve VSCF operation. The initial development and widespread use of the doubly fed induction machine (DFIM) can attribute to its cost-effectiveness and high controllability. However, conventional DFIMs rely on controlling the windings on the rotor to regulate the output frequency, necessitating the use of wound-rotor and slip rings. The slip ring mechanism presents challenges related to direct mechanical contact, which requires regular maintenance due to wear and tear.

To overcome the mechanical structure-related issues, several brushless doubly fed machine (BLDFM) have been proposed, including self-cascaded DFIM [4], dual-stator DFIMs [5, 6], nest-loop rotor based DFIM [7, 8], and brushless double fed reluctance machine (DFRM) [9, 10]. Nevertheless, many of these brushless structures suffer from drawbacks such as low power density and low efficiency.

Recent advancements in flux modulation theory have facilitated the development of brushless dual-electrical-port dual-mechanical-port DFMs (BLDD-DFMs). These machines eliminate the need for slip ring structures, thereby operating as brushless systems. BLDD-DFMs can be categorized into two types based on their operating principles [11]. The first type is the transverse-flux (TF) type, which integrates the transverse-flux machine (TFM) and the permanent magnet synchronous machine (PMSM) [12, 13]. However, the TFM faces manufacturing challenges that limit its widespread adoption. The second type is the magnetic-geared (MG) type, which is more commonly used due to its superior performance. It comprises a magnetic-geared machine (MGM) and a PMSM section. The PMSM generates power, while the MGM maintains a constant output frequency. Conventionally, a design is proposed where the stator and inner rotor constitute the PMSM section with the outer rotor positioned between them, results in a longer flux path for the PMSM, thereby reducing performance [14]. To address this issue, [15, 16]

Manuscript received Month xx, 2xxx; revised Month xx, xxxx; accepted Month x, xxxx. This work was supported in part by the … Department of xxx under Grant. *(Corresponding author: Shuangxia Niu.)*

Mingyuan Jiang, Shuangxia Niu and C.C. Chan are with the Department of Electrical and Electronic Engineering, The Hong Kong Polytechnic University, Hong Kong, 999077, China (e-mail: mingyuan.jiang@connect.polyu.hk; eesxniu@polyu.edu.hk; c.c.chan@polyu.edu.hk).

propose and analyze a dual-PM bidirectional flux modulation structure featuring two consequent-pole PM rotors. These designs enhance the PMSM performance by configuring the stator and outer rotor as the PMSM section. Furthermore, [17, 18] introduce spoke PMs as replacements for radial PMs on the outer rotor, further shortening the flux path and improving the torque density of the PMSM section. Another design in [19] suggests substituting the PMSM section with a permanent magnet Vernier machine (PMVM) section, enhancing power generation performance.

However, the MGM section, responsible for frequency control in BLDFMs, often exhibits low torque density due to limited utilization of flux harmonics, an aspect that has received limited attention in the industry. Improving the performance of the MGM section can result in energy savings in the control system and overall system efficiency enhancement.

In [20], a novel high-order harmonic winding design is proposed for the Vernier reluctance machine. The authors design a novel winding using the harmonics higher than the fundamental one, i.e., the high-order harmonic winding. A brushless dual-electrical-port dual-mechanical-port machine (BLDDM) based on the high-order harmonic is designed in [21] to further enhance the torque density of the MGM part while maintaining the same amount of PM material.

This paper extends the previously mentioned concept by introducing a novel BLDD-DFM structure for VSCF wind power applications. The proposed structure utilizes high-order harmonic modulation to reduce energy consumption in the control winding. The key is to artificially enhance the third-harmonic component of the airgap flux density within the inner airgap while keeping the fundamental component unchanged in the outer airgap. Both components are effectively utilized by the two windings incorporated in this design. The paper is organized as follows. In Sections II and III, the machine structure and the operating principle are introduced. In Section IV, the proposed BLDDM is compared with the conventional design in other literature in terms of the torque and working principle. In Section V, a prototype is made, and the experiment results verify the feasibility and advantages of the proposed design. Finally, conclusions are drawn in Section VI.

II. Machine Structure

Fig. 1 shows the proposed BLDD-DFM based wind power generation system, which is composed of two electrical ports and two mechanical ports, viz. two sets of stator winding and two concentric rotors. The stator has 24 slots, where the 2-pole-pair control winding and the 11-pole-pair power winding are placed inside. The inner rotor is connected with the wind turbine directly. It consists of only 31 iron teeth, which shows good mechanical robustness.

The outer rotor operates in idle. It has 11 pole pairs of spoke-type PMs and 11 pole pairs of radially-magnetized PMs, shown in Fig. 2. The iron core of the outer rotor is placed between two adjacent spoke PMs, and the radially-magnetized PM is placed in the duct along the inner side of the outer rotor. The radial-magnetized PMs are used to enhance the third harmonic component magnetomotive force (MMF) in the inner airgap, while remaining the fundamental component in the outer airgap. As the MMF in the outer airgap is used for the interaction with the regular winding and the MMF in the inner airgap is used for the flux modulation with the inner rotor, the fundamental and its third harmonic components can all be fully used in this design.

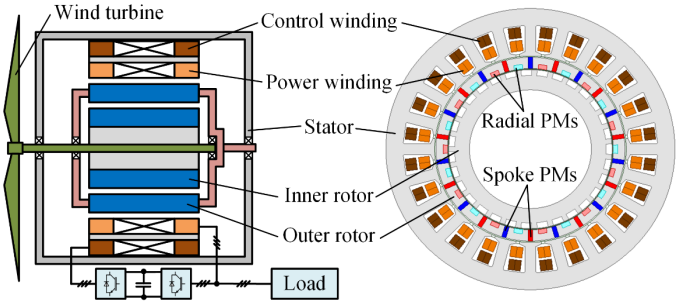

Fig. 1. The configuration of the BLDD-DFM based wind power generation system.

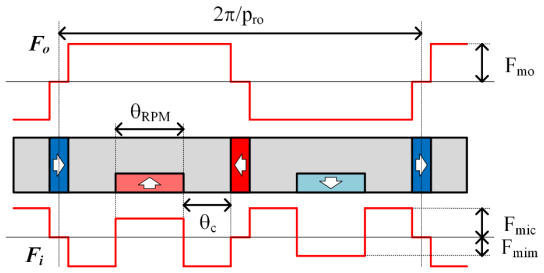

Fig. 2. The configuration of the outer rotor and the MMF in the inner and outer airgap.

The power winding connects to the grid directly, and the control winding connects to the grid via a back-to-back converter. The BLDD-DFM system can be regarded as the combination of a magnetic-geared control machine (MGCM) and a PM synchronous generator (PMSG). The outer rotor, inner rotor, and control winding form the MGCM. By controlling the frequency of control winding, the outer rotor can rotate in a fixed speed with random inner rotor speed. The PMSG is composed of the outer rotor and the power winding, which outputs power in constant frequency. Therefore, the VSCF control is achieved.

III. Operating Principle

A. MEC analysis

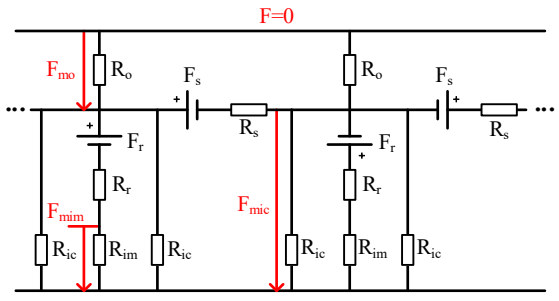

Fig. 3. The magnetic circuit of outer rotor.

The MMF waveforms excited by the PMs in the inner and outer airgap with the notations are shown in Fig. 2. To quantitively analyze the MMF waveform, when neglecting the magnetic resistance in iron core, the magnetic equivalent circuit (MEC) can be drawn in Fig. 3 [21, 22], where R_o, R_{ic}, and R_{im} are the magnetic resistance of outer airgap, inner airgap under the iron core section, and inner airgap under the PM section, R_s and R_r are the internal magnetic resistance of spoke-type PM and radially-magnetized PM, F_s and F_r are the MMF of spoke-type PM and radially-magnetized PM.

For the convenience of analyzing, the magnetic potential of the outer iron ring is set as zero. Based on Kirchhoff's law, the following relationship can be written in the matrix form $\mathbf{AF} = \mathbf{B}$:

$$\begin{bmatrix} \frac{1}{R_0}+\frac{4}{R_s} & \frac{2}{R_{ic}} & -\frac{1}{R_{im}} \\ 0 & 1 & 1+\frac{R_r}{R_{im}} \\ 2 & -2 & 0 \end{bmatrix} \begin{bmatrix} F_{mo} \\ F_{mic} \\ F_{mim} \end{bmatrix} = \begin{bmatrix} \frac{2F_s}{R_s} \\ F_r \\ 0 \end{bmatrix} \tag{1}$$

Therefore, the amplitude matrix $\mathbf{F}$ can be calculated:

$$\mathbf{F} = \begin{bmatrix} F_{mo} \\ F_{mic} \\ F_{mim} \end{bmatrix} = \mathbf{A^{-1}B} = \frac{1}{R_{sum}} \cdot \begin{bmatrix} R_{ic}R_o(2F_sR_{im}+F_rR_s+2F_sR_r) \\ R_{ic}R_o(2F_sR_{im}+F_rR_s+2F_sR_r) \\ R_{im}(4F_rR_{ic}R_o-2F_sR_{ic}R_o+F_rR_{ic}R_s+2F_rR_oR_s) \end{bmatrix} \tag{2}$$

$$R_{sum} = \frac{R_{ic}R_{im}R_oR_s}{2}\det(\mathbf{A}) \tag{3}$$

From Fig. 2, the MMF in the inner and outer airgap can be expressed by Fourier series as

$$F_i(\theta,t) = \sum_{n=1,odd}^{+\infty} F_{in}\cos(np_{ro}(\theta+\Omega_{ro}t)+\varphi) \tag{4}$$

$$F_o(\theta,t) = \sum_{m=1,odd}^{+\infty} F_{om}\cos(mp_{ro}(\theta+\Omega_{ro}t)+\varphi) \tag{5}$$

where p_{ro} is the pole pair number (PPN) of the outer rotor, which is also the PPN for both radially-magnetized and spoke-type PMs on the outer rotor, Ω_{ro} is the rotating speed of the outer rotor, φ is the initial angle of the outer rotor. F_{in} and F_{on} are the corresponding magnitude of the n-th and m-th MMF components, which can be further expressed by means of Fourier decomposition as

$$F_{in} = \frac{8F_{mic}}{n\pi}\sin\left(np_{ro}\frac{\theta_c}{2}\right)\cos\left(np_{ro}\frac{\theta_{RPM}+\theta_c}{2}\right) - \frac{4F_{mim}}{n\pi}\sin\left(np_{ro}\frac{\theta_{RPM}}{2}\right) \tag{6}$$

$$F_{om} = \frac{4F_{mo}}{m\pi}\sin\left(mp_{ro}\frac{2\theta_c+\theta_{RPM}}{2}\right) \tag{7}$$

B. MGCM part analysis

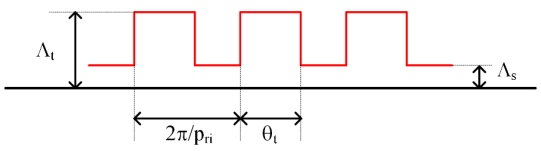

Fig. 4. Permeance waveform of the inner rotor.

The permeance waveform of the inner rotor in the inner airgap is shown in Fig. 4, which can be given as

$$\Lambda(\theta,t) = \frac{\Lambda_0}{2} + \sum_{k=1}^{+\infty}\Lambda_k\cos\left(kp_{ri}(\theta+\Omega_{ri}t)\right) \tag{8}$$

where p_{ri} is the number of the inner rotor's salient poles, Ω_{ri} is the rotating speed of the inner rotor, and Λ_k is the magnitude of the k-th permeance component, which can be expressed by Fourier decomposition as

$$\Lambda_k = \begin{cases} 2\Lambda_s + \frac{\theta_t p_{ri}}{\pi}(\Lambda_t-\Lambda_s), & k=0 \\ \frac{2(\Lambda_t-\Lambda_s)}{k\pi}\sin\left(\frac{kp_{ri}\theta_t}{2}\right), & k>0 \end{cases} \tag{9}$$

The airgap flux density of the MGCM part equals to the product of F_i and Λ, which can be expressed as

$$\begin{aligned} B_{MGCM}(\theta,t) &= F_i(\theta,t)\Lambda(\theta,t) \\ &= \sum_{n=1,odd}^{+\infty}\sum_{l=-\infty}^{+\infty}\frac{F_{in}\Lambda_l}{2}\cos((np_{ro}+lp_{ri}) \\ &=\cdot\left(\theta+\frac{np_{ro}\Omega_{ro}+lp_{ri}\Omega_{ri}}{np_{ro}+lp_{ri}}t\right)+\varphi) \end{aligned} \tag{10}$$

where

$$l = \pm k, \Lambda_l = \Lambda_{-l} \tag{11}$$

The PPN of the modulation winding p_{wm} should match the PPN of the modulated harmonic that generates the largest back EMF for maximum steady torque transformation. In the proposed design, p_{wc} is selected as the component that is modulated by the third harmonic, because the flux density and the speed of the third harmonic component are both higher than that of the fundamental one [20, 21]. According to (10), the PPN, speed, and the frequency of the control winding can be expressed as

$$p_{wc} = |np_{ro}+lp_{ri}|_{n=3,l=-1} = |3p_{ro}-p_{ri}| \tag{12}$$

$$\begin{aligned} \Omega_{wc} &= \left(\frac{np_{ro}}{np_{ro}+lp_{ri}}\Omega_{ro}+\frac{lp_{ri}}{np_{ro}+lp_{ri}}\Omega_{ri}\right)_{n=3,l=-1} \\ &= \frac{3p_{ro}\Omega_{ro}-p_{ri}\Omega_{ri}}{3p_{ro}-p_{ri}} \end{aligned} \tag{13}$$

$$f_{wc} = \frac{3p_{ro}\Omega_{ro}-p_{ri}\Omega_{ri}}{60} \tag{14}$$

C. PMSG part analysis

The spoke-type PMs enable the magnetic circuit to get through only the outer airgap, which has greatly decreased the magnetic reluctance [22]. The configuration of PMs on the outer rotor also has the flux-focusing effect, which increases the flux density in the airgap.

As the stator can be considered as a slotless iron core, its permeance only consists of the average component Λ_{st0}, and the airgap flux density of the PMSG part can be expressed as the following based on (5):

$$B_{PMSG}(\theta,t) = \sum_{m=1,odd}^{+\infty}F_{om}\Lambda_{st0}\cos(mp_{ro}(\theta+\Omega_{ro}t)+\varphi) \tag{15}$$

From (7) and (15), the largest component can be obtained when $m=1$. For generating the largest back EMF, the PPN speed, and the frequency of the power winding should satisfy

$$p_{wp} = (mp_{ro})_{m=1} = p_{ro} \tag{16}$$

$$\Omega_{wp} = \Omega_{ro} \tag{17}$$

$$f_{wp} = \frac{p_{ro}\Omega_{ro}}{60} \tag{18}$$

From (14) and (18), by controlling the frequency of the control winding, the outer rotor speed can remain constant despite variations in the inner rotor speed, and the frequency of power winding can remain constant, which achieved VSCF operation.

For shortening the end winding and reducing the cogging torque, the concentrated winding is often used, where the following relationship of p_{ro} and the slot number of stator Z in this paper is:

$$p_{ro} = p_{wp} = \frac{Z}{2} \pm 1 \tag{19}$$

D. Torque/Power distribution

Based on the torque balance equation and the law of energy conservation, the torque and power relationship of the MGCM part can be given as

$$T_{wc} + T_{roc} + T_{ri} = 0 \tag{20}$$

$$T_{wc}\Omega_{wc} + T_{roc}\Omega_{ro} + T_{ri}\Omega_{ri} = P_{wc} + P_{roc} + P_{ri} = 0 \tag{21}$$

where T_{wc} and T_{roc} are the electromagnetic torque and the outer rotor torque produced by the control winding, P_{wc} and P_{roc} are the electromagnetic power and the outer rotor power produced by the control winding, T_{ri} and P_{ri} are the inner rotor torque and power. With (12), (13), (20) and (21), the following torque-pole pair relationship can be obtained:

$$T_{wc}: T_{roc}: T_{ri} = p_{wc}: (-3p_{ro}): p_{ri} \tag{22}$$

Similarly, the torque and power relationship of the PMSG part can be expressed as

$$T_{wp} + T_{rop} = 0 \tag{23}$$

$$T_{wp}\Omega_{ro} + T_{rop}\Omega_{ro} = P_{wp} + P_{rop} = 0 \tag{24}$$

where T_{wp} and T_{rop} are the electromagnetic torque and the outer rotor torque produced by the power winding, P_{wp} and P_{rop} are the electromagnetic power and the outer rotor power produced by the power winding.

E. BLDFM analysis

For VSCF operation, the overall torque of the outer rotor T_{ro} should be 0, which can be given as

$$T_{ro} = T_{rop} + T_{roc} = 0 \tag{25}$$

Take (25) into (21) and (24), the following power relationship can be concluded:

$$P_{wc} + P_{ri} + P_{wp} = 0 \tag{26}$$

Here, defining the synchronous speed of inner rotor Ω_{ri0} as the speed when the control winding's input is direct current (DC), i.e., $f_{wc} = 0$, which can be expressed as

$$\Omega_{ri0} = \frac{3p_{ro}\Omega_{ro}}{p_{ri}} \tag{27}$$

From (12) – (18) and (27), the slip of the inner rotor can be given as

$$s = \frac{\Omega_{ri0} - \Omega_{ri}}{\Omega_{ri0}} = \frac{1}{3}\frac{p_{wc}\Omega_{wc}}{p_{wp}\Omega_{wp}} = \frac{1}{3}\frac{f_{wc}}{f_{wp}} \tag{28}$$

Take (22) and (23) into (28), the power of the control and power winding have the relationship of

$$\frac{P_{wc}}{P_{wp}} = \frac{T_{wc}\Omega_{wc}}{T_{wp}\Omega_{ro}} = \frac{p_{wc}\Omega_{wc}}{-3p_{ro}\Omega_{wp}} = -s \tag{29}$$

The negative sign shows the direction of control and power winding power is different, i.e., one input and one output. The input and output power for the BLDFM system are

$$P_{in} = P_{ri} \tag{30}$$

$$P_{out} = P_{wp} \tag{31}$$

Take (29) – (31) into (26), the relationship of input and output power can be given as

$$P_{in} = -(1-s)P_{out} \tag{32}$$

This shows the presented BLDFM system agrees with the concept of conventional DFM.

From (29), (31) and (32), the relationship of power winding and input power is

$$P_{wc} = -sP_{out} = \frac{s}{1-s}P_{in} \tag{33}$$

For conventional BLDD-DFM in [19] whose control winding choose to modulate with fundamental harmonic, the slip of the inner rotor is

$$s' = \frac{f_{wc}}{f_{wp}} = 3s \tag{34}$$

From (34), it can be observed that the slip of conventional design is three times of the proposed one. Therefore, take (34) into (33), the ratio of power consumption for the conventional power winding P'_{wc} and proposed power winding can be expressed as

$$\frac{P'_{wc}}{P_{wc}} = 3\frac{1-s}{1-3s} \tag{35}$$

For normal condition, the slip of both conventional and proposed designs should be in the range of [0,1], i.e.,

$$\begin{cases} s' \in [0,1] \\ s \in [0,1] \end{cases} \Rightarrow s \in \left[0, \frac{1}{3}\right] \tag{36}$$

Take (36) to (35), we can get

$$\frac{P'_{wc}}{P_{wc}} \in [3, +\infty] \tag{37}$$

From (37), it can be observed that when the input power remains the same, to achieve the same performance, the power consumption of the conventional design is at least 3 times greater than that of the proposed design, which is more energy efficient.

IV. Performance Analysis and Comparison

Table I

Main dimensions of the proposed design and conventional design

Item	Prop. BLDD-DFM	Conv. BLDD-DFM
Stator outer diameter	210 mm	
Stack length	50 mm	
Airgap length	1 mm	
Slot number (Z)	24	18
PPN of outer rotor spoke-PMs (p_{ro})	11	15
PPN of outer rotor radial-PMs	11	N/A
No. of inner rotor teeth (p_{ri})	31	13
PPN of control winding (p_{wc})	2	2
PPN of power winding (p_{wp})	11	3
PM volume	79.2 cm ^{3}	
Outer rotor speed	300 rpm	
Inner rotor speed	50 rpm	
Net slot area	125 mm^2	

Rated current density	6 A/mm^2
Magnet material	N40UH
Silicon steel sheet	35WW300

In order to demonstrate the enhancements provided by the proposed BLDD-DFM, two models were developed: the proposed model and a conventional model based on the design presented in [19]. The electromagnetic performances of these two machines were compared using FEM analysis. To ensure a fair and meaningful comparison, the net slot area, PM volume, and overall machine volume are kept identical for both designs. This paper use the optimization procedure based on NSGA-II in [21] , and the key dimensions of the two models are provided in Table I. In the subsequent tables and figures, the short terms "prop." and "conv." correspond to the proposed and conventional designs, respectively.

A. No-load Comparison and Analysis

The flux line distributions are depicted in the upper section of Fig. 5. In Fig. 5(a) and Fig. 5(b), a 2-pole-pair modulated field is observed in the inner rotor. The flux lines in the stator exhibit a combination of a 2-pole-pair and an 11-pole-pair field in Fig. 5(a), and a combination of a 2-pole-pair and a 3-pole-pair field is displayed in Fig. 5(b).

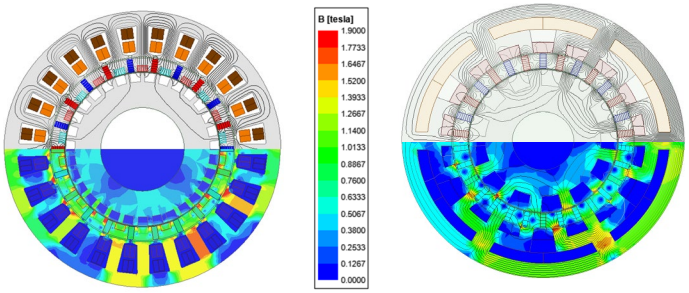

(a) (b)

Fig. 5. Comparison of no-load flux line distribution and on-load flux density map. (a) Proposed design. (b) Conventional design in [19].

Fig. 6 shows the airgap flux density waveforms and the harmonic distribution of the proposed and conventional designs in the outer airgap. The back EMF waveforms and their harmonic distributions of the proposed and conventional designs for the power and control windings are shown in Fig. 7 and Fig. 8, respectively.

Fig. 6 reveals that the dominant components that align with the control winding and power winding of the proposed design are the 2nd and 11th components, while the dominant components corresponding to the control winding and power winding of the conventional design are the 2nd and 3rd components. The 3rd component of flux density exhibits an amplitude of 0.17T. Although the 3rd component for the conventional design represents a flux modulated component with a higher frequency (five times the frequency of the proposed design due to the gear ratio of $G = \frac{p_{wp}}{p_{ro}} = 5$), its amplitude is comparatively lower. In contrast, the 11th component of the proposed design exhibits a significantly higher amplitude of 0.91T. As the back EMF is related to the product of winding factor, amplitude of flux, and frequency, and since the winding factor of both design are the same, the proposed design is better than the conventional design. In Fig. 7, the back EMF of the proposed design is 73% greater than that of the conventional design.

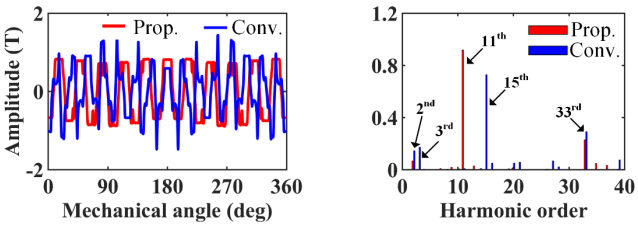

(a) (b)

Fig. 6. Comparison of the outer airgap flux density. (a) Waveform. (b) FFT spectrums.

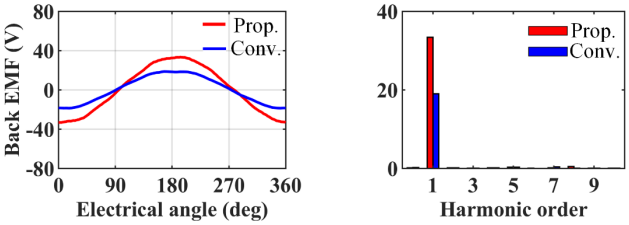

(a) (b)

Fig. 7. Comparison of power winding back EMF. (a) Waveform. (b) FFT spectrums.

In the proposed design, the amplitude of the 2nd component is 0.07T, which is slightly lower than the conventional design's amplitude of 0.14T. However, it is important to note that the field rotation speed of the proposed design is three times higher compared to the conventional design. This is because the salient teeth modulation primarily affects the third-harmonic component. Additionally, the pole pair number of both the inner and outer rotor in the conventional design is considerably smaller than that of the proposed design. Consequently, the frequency of the control winding in the proposed design is significantly higher. Hence, the back EMF of the proposed design is approximately five times greater than that of the conventional design, as depicted in Fig. 8. This results also agrees with (37).

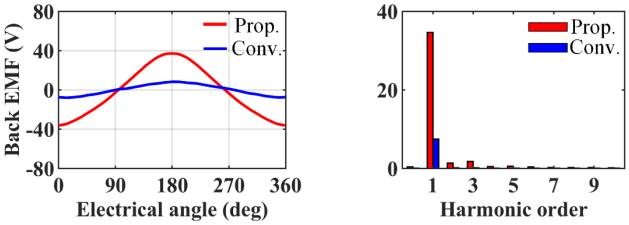

(a) (b)

Fig. 8. Comparison of control winding back EMF. (a) Waveform. (b) FFT spectrums.

B. On-load Comparison and Analysis

The flux density map of the two designs is presented in the lower section of Fig. 5. Both windings in both designs exhibit a current density of 6A/mm², which is suitable for air cooling. The maximum flux density observed in the stator teeth body and yoke of both designs remains below 1.7T, which is well below the knee point of the silicon steel sheet. It is worth noting that there are some localized areas of saturation on the

tooth tips due to the trade-off between limited tip geometry size and larger slot area. However, the impact of these saturation areas on the main flux is relatively small and can be considered negligible, given their limited extent.

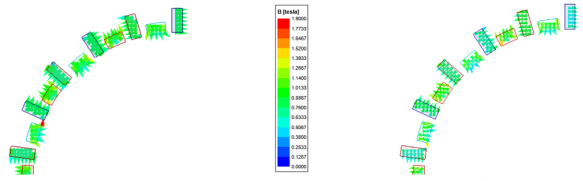

(a) (b)

Fig. 9. Flux density vectors at no load and full load condition. (a) No load. (b) Full load.

Fig. 9 displays the flux density vectors under both no load and full load conditions. The knee point of irreversible demagnetization for N40UH magnets at a temperature of 120˚C is determined to be -0.27 T. This indicates that when PMs undergo demagnetization, the direction of the flux density vector becomes opposite to the original magnetization direction. However, upon examining Fig. 9, it is evident that all flux density vectors align with the PMs, indicating the absence of demagnetization.

Fig. 10 to Fig. 13 display the torque density and the corresponding torque ripple of the outer and inner rotors for both the proposed and conventional designs under varying current in the power and control windings. In these figures, the current densities of the power and control windings are denoted as J_{wp} and J_{wc}, respectively. The torque density K_T and torque ripple T_{rip} are defined as

$$K_T = \frac{avg(T_r)}{V} \tag{38}$$

$$T_{rip} = \frac{pk2pk(T_r)}{avg(T_r)} \tag{39}$$

where $avg()$ is the function of calculation the average value, V is the electromagnetic part volume of the machine, and $pk2pk()$ is the function to compute the peak-to-peak value of the ripple.

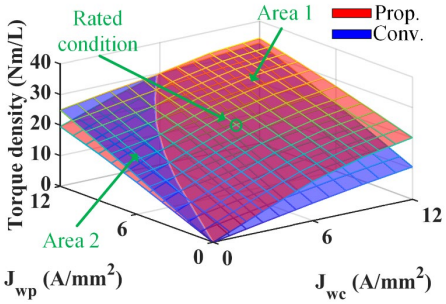

Fig. 10. Comparison of the outer rotor torque density.

Fig. 10 presents a comparison of the torque density for the outer rotor. In area 1, it is evident that the proposed design exhibits higher torque density than the conventional design under both rated and most operating conditions. The torque improvement variation reaches 23.03% under the rated condition, while the maximum variation reaches 122.59%. In area 2, the torque contribution from the MGCM portion is relatively small due to the low J_{wc} value. Consequently, the torque density of the proposed design is lower than that of the conventional design in this region. However, the maximum variation in area 2 is 21.69%, which is relatively smaller compared to the maximum variation observed in area 1.

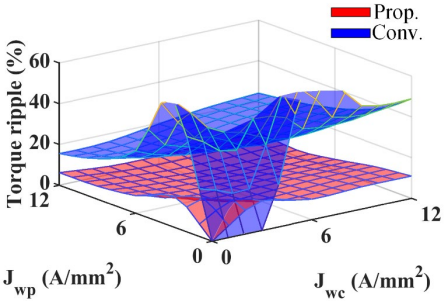

Fig. 11. Comparison of the outer rotor torque ripple.

Fig. 11 displays the torque ripple comparison for the outer rotor. In the proposed design, the mean torque ripple is 6.69%, with a value of 5.35% under the rated condition, and the maximum torque ripple reaches 15.15%. On the other hand, the conventional design exhibits a mean torque ripple of 28.89%, with a rated condition value of 23.83%, and a maximum torque ripple of 73.73%. The torque ripple of the proposed design is significantly lower than that of the conventional design, potentially attributed to factors such as the open-slot structure and the presence of abundant harmonics.

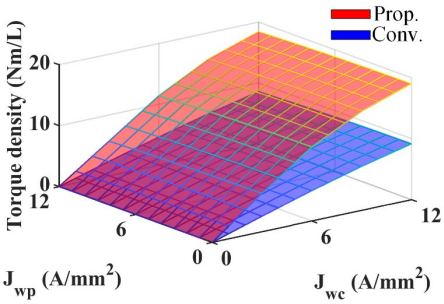

Fig. 12. Comparison of the inner rotor torque density.

From Fig. 12, it is evident that the torque density of the proposed design surpasses that of the conventional design across different J_{wc} values. It is important to note that J_{wp} solely affects the torque of the PMSG portion of the outer rotor and does not have any impact on the torque of the inner rotor. The torque improvement variation reaches 144.08% under the rated condition.

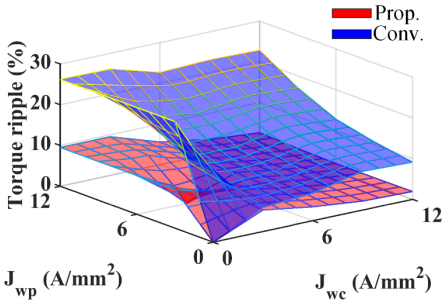

Fig. 13. Comparison of the inner rotor torque ripple.

Fig. 13 presents a comparison of the torque ripple for the inner rotor. In the proposed design, the mean torque ripple is 4.68%, with a maximum torque ripple of 9.53%. It is

noteworthy that all torque ripple values of the proposed design remain below 10%. Conversely, the conventional design demonstrates a mean torque ripple of 15.46%, with a maximum torque ripple of 26.20%. The torque ripple of the proposed design is notably lower than that of the conventional design, even for the inner rotor.

In the rated condition, the efficiencies of the proposed and conventional designs are both high, which are 92% and 93%, respectively. The power factor comparison of the proposed and conventional designs' power and control windings are presented in Fig. 14. For the power winding, both designs' power factors are relatively high in the rated condition, which are 0.89 and 0.88, respectively. For the control winding, both designs' power factors are relatively low, which are 0.51 and 0.43 under the rated condition. The reason for the low power factor is related to the common problem of the flux modulated machine, which are mainly caused by the flux leakage due to two airgaps and high gear ratio [23]. How to maintain high torque ratio while remain high power factor will be further investigated in the future.

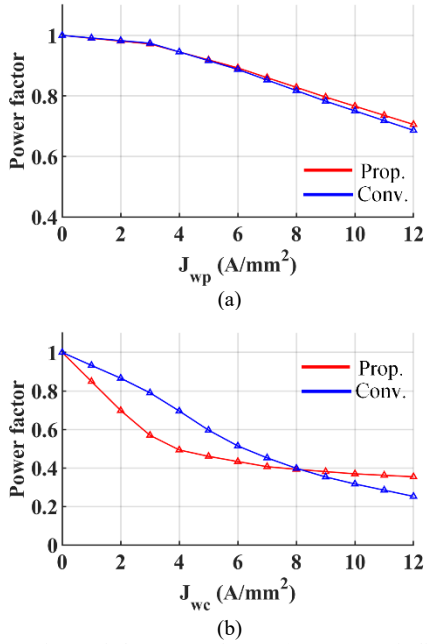

Fig. 14. Comparison of the power factor. (a) Power winding. (b) Control winding.

TABLE II
COMPARISON OF THE CONTROL WINDING POWER

Item	Prop. design	Conv. design
Outer rotor torque	25.22 Nm	9.09 Nm
Inner rotor torque	23.69Nm	7.88 Nm
Outer rotor speed	300 rpm	
Inner rotor speed	50 rpm	
Control winding power	916.18 W	326.77 W

The comparison of the control winding power at the rated speed are listed in Table II. The proposed design exhibits significantly higher power output in the control winding compared to the conventional design when injecting an equivalent current. Specifically, the control winding power of the proposed design is 2.8 times greater than that of the conventional design. Consequently, to achieve comparable performance, the power consumption of the proposed design is approximately one-third of that required by the conventional design.

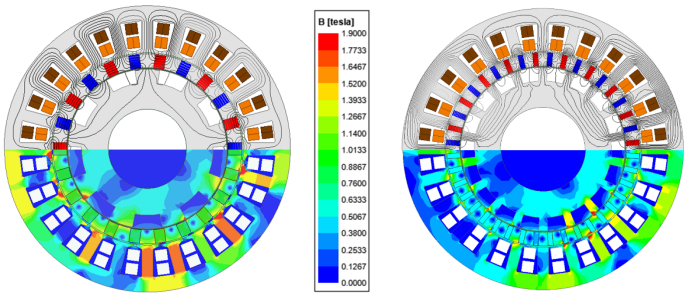

Fig. 15. The no-load flux line distribution and on-load flux density map of the designs with similar structure. (a) Design based on [22] (PMSM + fundamental harmonic based MGM). (b) Design based on [23] (low gear ratio PMVM + low gear ratio MGM).

TABLE III
MAIN DIMENSIONS OF THE PROPOSED DESIGN AND DESIGNS WITH SIMIALR STRUCTURE

Item	Prop. design	Design based on [22]	Design based on [23]
Stator outer diameter		210 mm	
Stack length		50 mm	
Airgap length		1 mm	
Slot number (Z)		24	
PPN of outer rotor spoke-PMs (p_{ro})	11	11	20
PPN of outer rotor radial-PMs	11	N/A	N/A
No. of inner rotor teeth (p_{ri})	31	9	18
PPN of control winding		2	
PPN of power winding	11	11	4
PM volume		86.5 cm^3	
Outer rotor speed		300 rpm	
Inner rotor speed		50 rpm	
Net slot area		125 mm^2	
Rated current density		6 A/mm^2	
Magnet material		N40UH	
Silicon steel sheet		35WW300	

The comparison of the proposed design with the design with similar structure based on [22] and [23] has been conducted, where the dimensions are shown in Table III. The no-load flux line distribution and on-load flux density map of the design based on [22] and [23] are shown in Fig. 15. The design based on [22] can be considered as a combination of a PMSM and a fundamental harmonic based MGM, while the design based on [23] combines a low gear ratio PMVM and low gear ratio MGM. The comparison of the performances is listed in Table IV.

Based on the data provided in Table IV, it is observed that when the rotors operate at their rated speed and both windings reach the rated current density, a comparison between the proposed design and the conventional design based on [22] reveals several distinct characteristics. Firstly, the proposed design exhibits an approximately 8.70% lower fundamental amplitude of power winding back EMF and a 5.49% smaller torque in the PMSG portion compared to the conventional design. However, it is noteworthy that the no-load back EMF in the control winding and the torque generated by the MGCM

portion in the proposed design are 33.13% and 31.36% higher, respectively, when compared to the conventional design. These enhancements are primarily attributed to the utilization of high-order modulation in the proposed design [18]. Both designs demonstrate relatively small torque ripple, remaining below 15% of the average torque.

Compared to the conventional design based on [23], it can be found that the proposed design has around 5.5% lower fundamental amplitude of power winding back EMFs and 25.9% smaller PMSG portion torque than that of the conventional design, which are the result of higher frequency of the conventional design due to its vernier structure. The no-load back EMF in control winding is 4.27% higher, but the MGCM portion torque of the proposed design is 27.19% lower than the conventional design. This decrease in torque is primarily attributed to the higher flux leakage due to the high gear ratio. The selection of the gear ratio for the high-order modulation design will be further analyzed in the future study. Both designs exhibit relatively small torque ripple, which remains below 15% of the average torque.

TABLE IV
COMPARISON OF THE PERFORMANCE OF THE SIMILAR STRUCTURE

Item	Prop. design	Design based on [22]	Design based on [23]
Back EMF of power winding	33.36 V	36.54 V	35.30 V
Back EMF of control winding	34.62 V	23.15 V	33.14 V
PMSG portion torque	22.72 Nm	24.04 Nm	30.66 Nm
PMSG portion torque ripple	1.89 Nm (8.32%)	2.62 Nm (10.90%)	2.79 Nm (9.10%)
MGCM portion torque	25.22 Nm	17.31 Nm	34.64 Nm
MGCM portion torque ripple	3.28 Nm (13.01%)	1.57 Nm (9.07%)	3.91 Nm (11.29%)

V. EXPERIMENT VALIDATION

A prototype of the proposed BLDD-DFM is constructed to validate the feasibility, as depicted in Fig. 16. The detailed exploded view and cross section view of the proposed machine are shown in Fig. 16(a) and Fig. 16(b). In order to improve the mechanical robustness of the outer rotor, additional mounting holes with diameter of 3mm and a flux bridge with the width of 1mm are incorporated, as shown in Fig. 16(a). The left and right outer rotor frames are joined to the long nails to offer structural reinforcement to the outer rotor. The end cover on the right side is linked to the outer rotor shaft. Both rotor shafts are supported by bearings and the stator end caps, ensuring independent rotation of the inner rotor and outer rotor. The photos of the prototype assemblies are shown in Fig. 16(c).

For VSCF operation, an experimental setup was prepared, as illustrated in Fig. 17. A servo motor was connected to the inner rotor to simulate the input from a wind turbine in this particular scenario. The outer rotor was suspended in the air, and its shaft was extended to enable position measurement. The power winding was linked to a three-phase resistance network with a resistance of 10Ω, serving as the load. The control winding was connected to an inverter, controlled by a dSPACE controller that adjusted the speed of the inner rotor. Fig. 18 presents the control diagram, which employed conventional field-oriented control. The reference speed of the control winding is dynamically calculated based on (14).

Fig. 19 illustrates the noload back electromotive force (EMF) waveforms at an outer rotor speed of 300rpm and an inner rotor speed of 50rpm. Specifically, Fig. 19(a) and Fig. 19(b) present a comparison between the measured waveform (labelled "Exp.") and the finite element method (FEM) waveform for the control winding and power winding, respectively. The measured results obtained from the experiments are denoted as "Exp." in Fig. 19. The comparison demonstrates a good agreement between the experimental and FEM waveforms. The amplitude deviation is found to be 4.47% for the control winding and 1.83% for the power winding.

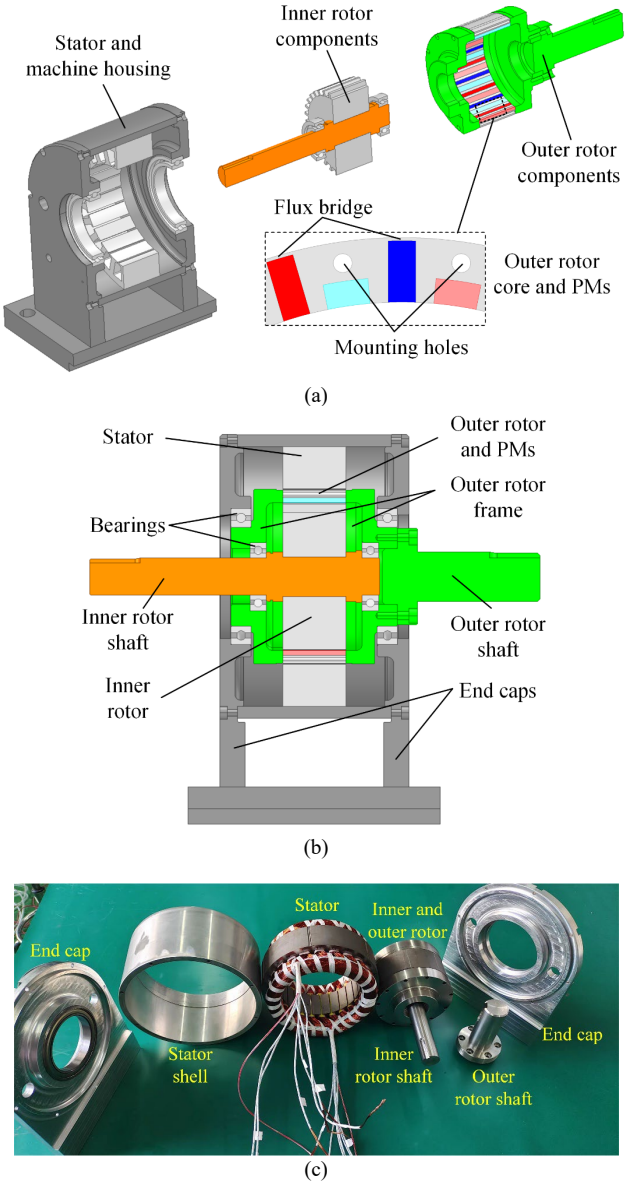

Fig. 16. Prototype assembly. (a) Exploded view. (b) Cross section view. (c) Photos.

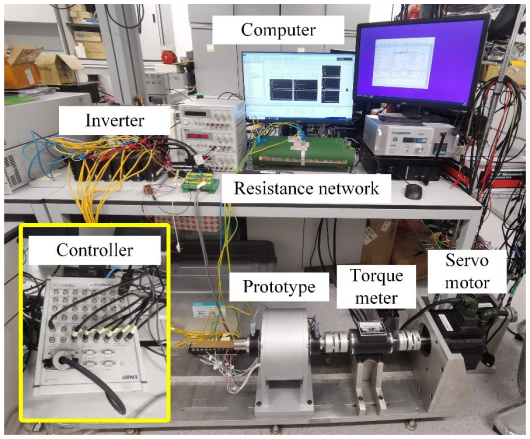

Fig. 17. Schematic of experiment setup.

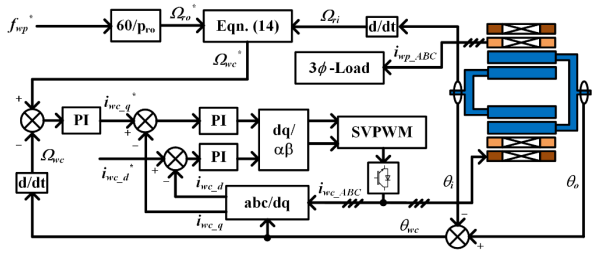

Fig. 18. Control diagram of the proposed BLDD-DFM.

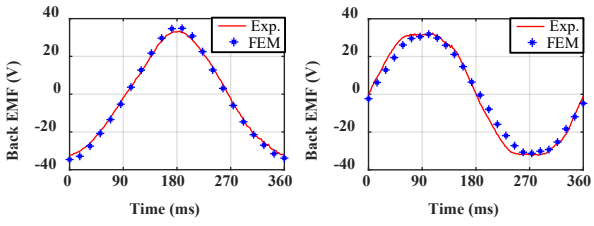

Fig. 19. No load back EMF waveforms. (a) Control winding. (b) Power winding.

The static VSCF experiment results are shown in Fig. 21, where "sub-syn.", "syn.", and "super-syn." refers to the sub-synchronous mode, synchronous mode, and super-synchronous mode. According to (17), (18) and (27), the synchronous speed of the inner rotor can be calculated as 290 rpm when the constant output frequency is set as 50Hz. When the inner rotor rotates at the speed of 200rpm, shown in Fig. 20(a), the control winding operates in sub-synchronous mode. The frequency of the winding is 47Hz with the positive sequence, i.e., Phase B leading Phase C by 120 electrical degrees, shown in the left subfigure of Fig. 20(c). When the inner rotor rotates at the synchronous speed, the frequency of the control winding changed to almost 0, shown in the middle part of Fig. 20(c). The control winding enters the super-synchronous mode when the inner rotor rotates at 360 rpm. The frequency at this mode is -35.85Hz, where the negative sign refers to the negative sequence, shown in the right subfigure of Fig. 20(c). At this state, Phase B is lagging Phase C by 120 electrical degrees. By changing the frequency of the control winding, the speed of outer rotor and the frequency of power winding remain constant regardless the changing input rotor speed, shown in Fig. 20(b) and Fig. 20(d), respectively.

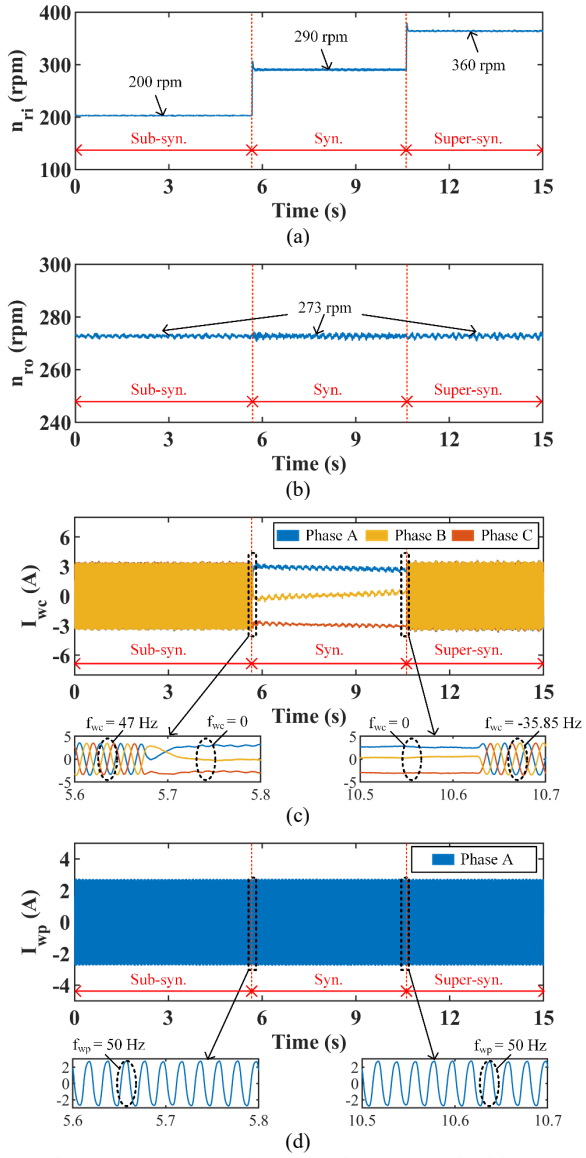

Fig. 20. The static VSCF experiment results. (a) Speed of inner rotor. (b) Speed of outer rotor. (c) Current of control winding. (d) Current of power winding.

The dynamic VSCF experiment results are shown in Fig. 21, where "Dyn. process" refers to dynamic process. From Fig. 21(a), the inner rotor speed increases linearly from sub-synchronous mode to super-synchronous mode. Accordingly, the frequency of the control winding is changing continuously during the dynamic process, and the current sequence can be clearly observed to be altered at 5.38s, shown in the right subfigure of Fig. 21(c). The inner rotor speed and the frequency of power winding also remain constant under the dynamic process, shown in Fig. 21(b) and Fig. 21(d), respectively.

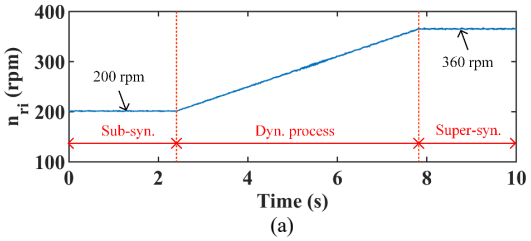

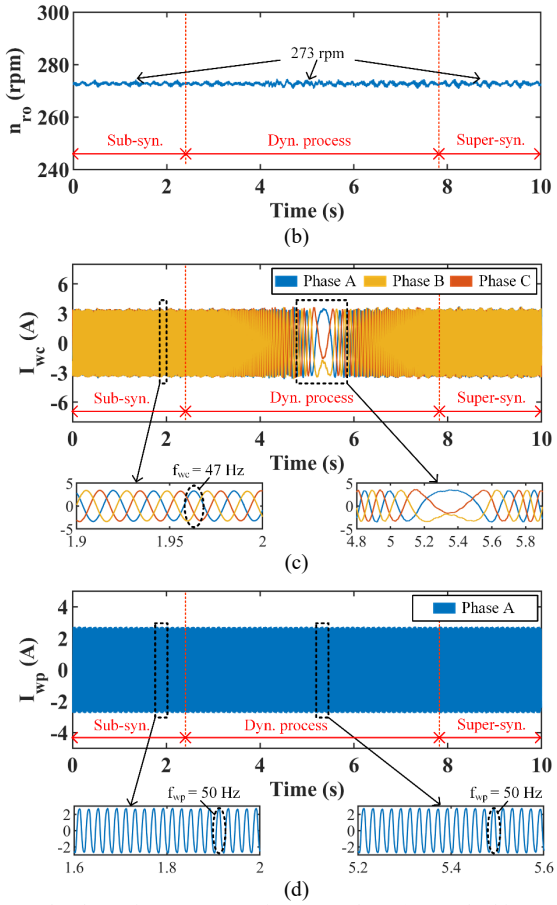

Fig. 21. The dynamic VSCF experiment results. (a) Speed of inner rotor. (b) Speed of outer rotor. (c) Current of control winding. (d) Current of power winding.

Fig. 22 displays the measured torque, current, and voltage waveforms corresponding to the inner rotor speeds of 200 and 360 rpm. As observed, the static torque remains constant at 4.7 and 4.9 Nm under the current load, exhibiting a maximum deviation of 4.65% when compared to the FEM analysis results. The torque ripple under two speeds is 7.64% and 8.25%, which both agree with the FEM with the maximum derivation of 4%. The frequency of the control winding varies along with the inner rotor speed. When the load remains unchanged, the amplitude of the power winding's current and voltage remains consistent during the VSCF operation.

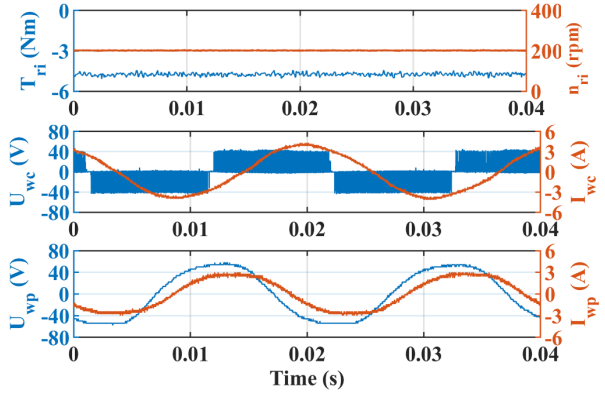

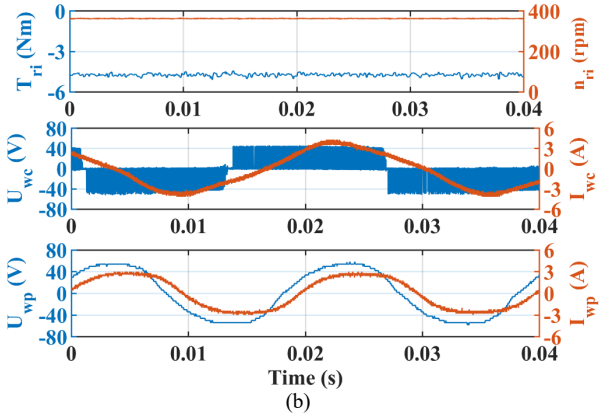

Fig. 22. Measured torque-current-voltage waveforms. (a) n_{ri} = 200 rpm. (b) n_{ri} = 360 rpm.

VI. Conclusion

This study introduces a novel BLDD-DFM structure that employs high-order harmonic modulation to enhance torque density in the MGCM portion and minimize energy consumption in the control winding. By utilizing high-order modulation in conjunction with a specialized outer rotor design, the slip ratio of the proposed design is significantly reduced, resulting in over a 3-fold reduction in energy consumption compared to conventional designs. FEM simulations are conducted to compare the prototype with a conventional design of similar dimensions. The results indicate that the back EMF in the control winding of the proposed design is five times greater than that of the conventional design and 73% higher than the power winding in the conventional design. Under rated conditions, the torque improvement in the proposed design reaches a maximum of 23.03% for the outer rotor torque and 144.08% for the inner rotor torque compared to the conventional design. Furthermore, the torque ripple of both the outer and inner rotors in the proposed design is approximately half that of the conventional design. A prototype is manufactured and tested, and the experimental results align with the working principles and FEM simulations. VSCF experiments conducted under static and dynamic conditions confirm the feasibility of the proposed design.

Acknowledgment

This work was supported by grants from National Natural Science Foundation of China, under Project NSFC 52077187.

References

[1] S. A. Vargas, G. R. T. Esteves, P. M. Maçaira, B. Q. Bastos, F. L. C. Oliveira, and R. C. Souza, "Wind power generation: A review and a research agenda," *Journal of Cleaner Production,* vol. 218, pp. 850-870, 2019.

[2] H. Polinder, J. A. Ferreira, B. B. Jensen, A. B. Abrahamsen, K. Atallah, and R. A. McMahon, "Trends in wind turbine generator systems," *IEEE Journal of emerging and selected topics in power electronics,* vol. 1, no. 3, pp. 174-185, 2013.

[3] Y. Tang and L. Xu, "A flexible active and reactive power control strategy for a variable speed constant frequency generating system," *IEEE Transactions on power electronics,* vol. 10, no. 4, pp. 472-478, 1995.

[4] A. Broadway and L. Burbridge, "Self-cascaded machine: a low-speed motor or high-frequency brushless alternator," in *Proceedings of the Institution of Electrical Engineers*, 1970, vol. 117, no. 7: IET, pp. 1277-1290.
[5] Y. Wang, S. L. Ho, W. Fu, and J. Shen, "A novel brushless doubly fed generator for wind power generation," *IEEE transactions on magnetics,* vol. 48, no. 11, pp. 4172-4175, 2012.
[6] P. Han, M. Cheng, Y. Jiang, and Z. Chen, "Torque/power density optimization of a dual-stator brushless doubly-fed induction generator for wind power application," *IEEE Transactions on Industrial electronics,* vol. 64, no. 12, pp. 9864-9875, 2017.
[7] M. Afshar, A. Tabesh, M. Ebrahimi, and S. A. Khajehoddin, "Stator short-circuit fault detection and location methods for brushless DFIMs using nested-loop rotor slot harmonics," *IEEE Transactions on Power Electronics,* vol. 35, no. 8, pp. 8559-8568, 2019.
[8] F. Barati, S. Shao, E. Abdi, H. Oraee, and R. McMahon, "Generalized vector model for the brushless doubly-fed machine with a nested-loop rotor," *IEEE Transactions on Industrial Electronics,* vol. 58, no. 6, pp. 2313-2321, 2010.
[9] A. Broadway, "Cageless induction machine," in *Proceedings of the Institution of Electrical Engineers*, 1971, vol. 118, no. 11: IET, pp. 1593-1600.
[10] P. Han, J. Zhang, and M. Cheng, "Analytical analysis and performance characterization of brushless doubly fed machines with multibarrier rotors," *IEEE Transactions on Industry Applications,* vol. 55, no. 6, pp. 5758-5767, 2019.
[11] M. Jiang and S. Niu, "Overview of Dual Mechanical Port Machines in Transportation Electrification," *IEEE Transactions on Transportation Electrification,* pp. 1-1, 2023, doi: 10.1109/tte.2023.3324948.
[12] C. Tong, P. Zheng, Q. Wu, J. Bai, and Q. Zhao, "A brushless claw-pole double-rotor machine for power-split hybrid electric vehicles," *IEEE Transactions on Industrial Electronics,* vol. 61, no. 8, pp. 4295-4305, 2013.
[13] M. Wang, P. Zheng, C. Tong, Q. Zhao, and G. Qiao, "Research on a transverse-flux brushless double-rotor machine for hybrid electric vehicles," *IEEE Transactions on Industrial Electronics,* vol. 66, no. 2, pp. 1032-1043, 2018.
[14] J. Zhang, Y. Jiang, X. Hu, and S. Xu, "A Brushless Doubly Fed Generator Based on Permanent Magnet Field Modulation," *IEEE Transactions on Industrial Electronics,* vol. 67, no. 5, pp. 3505-3516, 2020, doi: 10.1109/tie.2019.2916381.
[15] Y. Liu, S. Niu, and W. Fu, "Design of an electrical continuously variable transmission based wind energy conversion system," *IEEE Transactions on Industrial Electronics,* vol. 63, no. 11, pp. 6745-6755, 2016.
[16] Y. Wang, S. Niu, and W. Fu, "Sensitivity analysis and optimal design of a dual mechanical port bidirectional flux-modulated machine," *IEEE Transactions on Industrial Electronics,* vol. 65, no. 1, pp. 211-220, 2017.
[17] X. Ren, D. Li, R. Qu, and T. Zou, "A brushless dual-mechanical-port dual-electrical-port machine with spoke array magnets in flux modulator," *IEEE Transactions on Magnetics,* vol. 53, no. 11, pp. 1-6, 2017.
[18] X. Ren, D. Li, R. Qu, W. Kong, X. Han, and T. Pei, "Analysis of spoke-type brushless dual-electrical-port dual-mechanical-port machine with decoupled windings," *IEEE Transactions on Industrial Electronics,* vol. 66, no. 8, pp. 6128-6140, 2018.
[19] H. Chen *et al.*, "A Permanent Magnet Brushless Doubly Fed Electric Machine for Variable-Speed Constant-Frequency Wind Turbines," *IEEE Transactions on Industrial Electronics,* vol. 70, no. 7, pp. 6663-6674, 2023, doi: 10.1109/tie.2022.3201306.
[20] X. Zhao, S. Wang, S. Niu, W. Fu, and X. Zhang, "A Novel High-Order-Harmonic Winding Design Method for Vernier Reluctance Machine With DC Coils Across Two Stator Teeth," *IEEE Transactions on Industrial Electronics,* vol. 69, no. 8, pp. 7696-7707, 2022, doi: 10.1109/tie.2021.3104589.
[21] M. Jiang and S. Niu, "A High-Order Harmonic Compound Rotor Based Brushless Dual-Electrical-Port Dual-Mechanical-Port Machine," *IEEE Transactions on Industrial Electronics,* pp. 1-11, 2023, doi: 10.1109/tie.2023.3294574.
[22] Z. Liang, X. Ren, D. Li, R. Qu, and X. Han, "Analysis of a Spoke-Array Brushless Dual-Electrical-Port Dual-Mechanical-Port Machine With Reluctance Rotor," *IEEE Transactions on Industrial Electronics,* vol. 68, no. 4, pp. 2999-3011, 2021, doi: 10.1109/tie.2020.2982084.
[23] L. Cao *et al.*, "Analysis of Contra-Rotating Brushless Integrated Flux-Modulation Machine With Open-Slot Structure for Wind Power Generation," *IEEE Transactions on Industrial Electronics,* pp. 1-14, 2023, doi: 10.1109/tie.2023.3239901.

Mingyuan Jiang received the B.Eng. degree in electrical engineering and automation from Shanghai Maritime University, Shanghai, China, in 2020, and the M.Sc. and Ph.D. degrees in electrical engineering from The Hong Kong Polytechnic University, Hong Kong, China, in 2021 and 2024. His main research interests include design, optimization, and control of electric machines.

Shuangxia Niu (Senior Member, IEEE) received the B.Sc. and M.Sc. degrees from Tianjin University, Tianjin, China, in 2002 and 2005, and the Ph.D. degree from the University of Hong Kong, Hong Kong, SAR, China, in 2009, all in electrical engineering. She is currently a professor with the Department of Electrical and Electronic Engineering, The Hong Kong Polytechnic University. She authored or coauthored more than 200 papers in leading journals. Prof. Niu is currently an Associate Editor for the IEEE Journal of Emerging and Selected Topics in Power Electronics. She is Distinguish Lecturer of IEEE Vehicular Technology Society.

Ching Chuen Chan (Life Fellow, IEEE) was born in 1937. He received the B.S. degree from the China University of Mining and Technology, Xuzhou, China, the M.S. degree from Tsinghua University, Beijing, China, and the Ph.D. degree from The University of Hong Kong, Hong Kong, China, in 1957, 1959, and 1982, respectively, all in electrical engineering. He is currently a Distinguished Chair Professor of Electric Vehicles and Smart Energy with the Department of Electrical and Electronic Engineering, The Hong Kong Polytechnic University. He has more than 50 years of teaching and research experience and proposes engineering philosophy, engineering and education innovation, which laid the foundation of modern electric vehicles theory and electric vehicles electric drive theory. He has authored more than 300 papers and 11 monographs. Prof. Chan is a Member of Chinese Academy of Engineering, Fellow of the Royal Academy of Engineering U.K., Member of Ukrainian Academy of Engineering Sciences, and Honorary Fellow of Hungarian Academy of Engineering. He is senior IET Fellow, and the former President of the Hong Kong Institution of Engineers. He was the recipient of the Toastmasters Medal by the Institution of Electrical Engineers (IEE) in 2000, “Father of Asian Electric Vehicles” by Magazine Global View in 2003, “Environmental Excellence in Transportation Award” by the Society of Automotive Engineers (SAE) in 2007, Gold Medal of Hong Kong Institution of Engineers in 2010, World Federation of Engineering (WFEO) Medal for Engineering Excellence in 2013, Prince Philip Medal of UK Royal Academy of Engineering in 2014, and “IEEE Transportation Technologies Award” by the Institute of Electrical and Electronics Engineers (IEEE) in 2018.